

Temporal scale-dependent sensitivity analysis using discrete wavelet transform and active subspaces

Daniel Bittner¹, Michael Engel¹, Barbara Wohlmuth², David Labat³, and Gabriele Chiogna¹

¹Technical University Munich

²Technische Universität München

³Geosciences Environnement Toulouse

November 22, 2022

Abstract

Global sensitivity analysis of model parameters is an important step in the development of a hydrological model. If available, time series of different variables are used to increase the number of sensitive model parameters and better constrain the model output. However, this is often not possible. To overcome this problem, we coupled the active subspace method with the discrete wavelet transform. The Haar mother wavelet is the most appropriate for this purpose in case of homoschedastic measurement error, since it avoids any loss of information through the discrete wavelet transform of the signal. With this methodology, we study how the temporal scale dependency of hydrological processes affects the structure and dimension of the active subspaces. We apply the methodology to the LuKARS model of the Kerschbaum spring discharge in Waidhofen a.d. Ybbs (Austria). Our results reveal that the dimensionality of an active subspace increases with increasing hydrologic processes which are affecting a temporal scale. As a consequence, different parameters are sensitive on different temporal scales. Finally, we show that the total number of sensitive parameters identified at different temporal scales is larger than the number of sensitive parameters obtained using the complete spring discharge signal. Hence, instead of using multiple data time series to identify more sensitive parameters, we can also obtain more information about parameter sensitivities from one single, decomposed time series.

Temporal scale-dependent sensitivity analysis using discrete wavelet transform and active subspaces

Daniel Bittner¹, Michael Engel¹, Barbara Wohlmuth^{2,3}, David Labat⁴,
Gabriele Chiogna^{1,5}

¹Chair of Hydrology and River Basin Management, Technical University Munich,

Arcisstraße 21, 80333 Munich, Germany

²Chair for Numerical Mathematics, Technical University Munich, Boltzmannstraße 3, 85748 Garching
near Munich, Germany

³Department of Mathematics, University of Bergen, Allegaten 41, 5020 Bergen, Norway

⁴Geosciences Environnement Toulouse – GET, 14, Avenue Edouard Belin, 31400 Toulouse, France

⁵Institute of Geography, University of Innsbruck, Innrain 52, 6020 Innsbruck, Austria

Key Points:

- Results show that active subspaces are temporal scale dependent
- Active subspace dimensions reflect dominant hydrological processes on different temporal scales
- Methodology provides information on temporal-scale dependent parameter sensitivities

Abstract

Global sensitivity analysis of model parameters is an important step in the development of a hydrological model. If available, time series of different variables are used to increase the number of sensitive model parameters and better constrain the model output. However, this is often not possible. To overcome this problem, we coupled the active subspace method with the discrete wavelet transform. The Haar mother wavelet is the most appropriate for this purpose in case of homoschedastic measurement error, since it avoids any loss of information through the discrete wavelet transform of the signal. With this methodology, we study how the temporal scale dependency of hydrological processes affects the structure and dimension of the active subspaces. We apply the methodology to the LuKARS model of the Kerschbaum spring discharge in Waidhofen a.d. Ybbs (Austria). Our results reveal that the dimensionality of an active subspace increases with increasing hydrologic processes which are affecting a temporal scale. As a consequence,

Corresponding author: Gabriele Chiogna, gabriele.chiogna@tum.de

31 different parameters are sensitive on different temporal scales. Finally, we show that the
32 total number of sensitive parameters identified at different temporal scales is larger than
33 the number of sensitive parameters obtained using the complete spring discharge signal.
34 Hence, instead of using multiple data time series to identify more sensitive parameters,
35 we can also obtain more information about parameter sensitivities from one single, de-
36 composed time series.

37 **1 Introduction**

38 Uncertainty quantification constitutes an important part of hydrological modeling
39 (Hartmann et al., 2017; Wagener & Pianosi, 2019). In particular, quantifying paramet-
40 ric uncertainty is important since the reliability of simulation results strongly depends
41 on its parametrization (Beven, 1995; Reinecke et al., 2019). Within the context of para-
42 metric uncertainty, the determination of an appropriate parameter set is usually accom-
43 panied by sensitivity analyses (Borgonovo et al., 2017; Vrugt et al., 2002). Sensitivity
44 analysis measures how much the output of a model changes by varying its inputs, e.g.
45 spring discharge (van Werkhoven et al., 2008; Wagener & Montanari, 2011). Sensitiv-
46 ity analysis methods can be divided into two groups: local and global methods (Pianosi
47 et al., 2016; Saltelli et al., 2008). In a local sensitivity analysis, parameter modifications
48 are only performed at single locations of the parameter space (Tang et al., 2007; Saltelli
49 et al., 2019). In contrast, parameter sensitivity is measured over the full parameter space
50 in a global analysis (Razavi & Gupta, 2015; Song et al., 2015). Global methods are usu-
51 ally preferred in hydrology as they provide information on the sensitivity of one param-
52 eter in relation to others (Cloke et al., 2008; Wagener & Pianosi, 2019).

53 Constantine et al. (2014) and Constantine and Diaz (2017) proposed the active sub-
54 space method as a tool to perform global sensitivity analysis. Besides computing a global
55 sensitivity metric, this method has the advantage that it further provides information
56 on relevant linear combinations of model parameters. These relevant parameter combi-

57 nations can be used to efficiently construct surrogate models and perform Bayesian in-
58 version at low computational cost (Erdal & Cirpka, 2019; Teixeira Parente et al., 2019).
59 The active subspace method was successfully applied in several hydrological studies rang-
60 ing from lumped parameter models (Bittner, Teixeira Parente, et al., 2020; Teixeira Par-
61 ente et al., 2019) to distributed modeling approaches (Erdal & Cirpka, 2019, 2020; Gilbert
62 et al., 2016). (Bittner, Teixeira Parente, et al., 2020) also showed that the features and
63 dimension of an active subspace can find a reasonable hydrological explanation, in case
64 of a lumped karst hydrological model. So far, the active subspace method was applied
65 to hydrological variables that integrate processes occurring at multiple temporal scales,
66 such as discharge and heat fluxes (Erdal & Cirpka, 2020; Jefferson et al., 2015). How-
67 ever, it is well known that hydrological time series can be decomposed into different tem-
68 poral scales, for example using wavelet transform analysis (Grinsted et al., 2004; Labat
69 et al., 2000b; Torrence & Compo, 1998).

70 Wavelet transforms determine the crucial scales of variability and localizes varia-
71 tions in the modes of variability within a time series (Labat, 2005). In hydrology, both
72 continuous and discrete wavelet transform (Daubechies, 1990; Grinsted et al., 2004; Sang
73 et al., 2013; Torrence & Compo, 1998) have been traditionally used to analyze the main
74 scales of variability of time series (Carey et al., 2013; Coulibaly & Burn, 2004; Labat et
75 al., 2000b; Labat, 2005; Marcolini et al., 2017; Nalley et al., 2012), their coherence with
76 climatic and meteorological drivers (Jennings & Jones, 2015; Massei et al., 2010; Nal-
77 ley et al., 2016; Schaeffi et al., 2007), the impact of anthropogenic activities on the hy-
78 drological cycle (Pérez Ciria et al., 2019; Zolezzi et al., 2009), catchment classification
79 (Agarwal et al., 2016; Pérez Ciria & Chiogna, 2020) and change point analysis (Adamowski
80 & Prokoph, 2014). Less common is their application for the assessment of model per-
81 formance (Chiogna et al., 2018; Rathinasamy et al., 2014) and model calibration (Duran
82 et al., 2020; Schaeffi & Zehe, 2009). Although several choices of the generating function,
83 i.e. mother wavelet, are popular, it influences the resulting wavelet spectrum (Pérez Ciria
84 et al., 2019; Schaeffi et al., 2007). In particular, we focus on the decomposed signal us-

85 ing the discrete wavelet transform (DWT), since it is not possible to reconstruct the orig-
86 inal signal from the coefficients derived from the continuous wavelet transform (CWT)
87 analysis.

88 In this work, we study how temporal scale dependency of hydrological processes
89 affects the structure of the active subspaces and the computed parameter sensitivities.
90 Our hypothesis is that the active subspace dimension reflects how different linear com-
91 binations of model parameters control the simulated hydrological processes on multiple
92 temporal scales. Moreover, we hypothesize that the sensitive parameters differ for dif-
93 ferent temporal scales of the signal, and that they can be directly related to the dom-
94 inant hydrological processes of the respective temporal scales. To test these hypotheses,
95 we couple the active subspace method with the DWT. We apply our developed method-
96 ology to a lumped karst aquifer model, i.e. LuKARS (Land use change modeling in KARSt
97 systems), using data from the Kerschbaum springshed in Austria (Bittner et al., 2018;
98 Bittner, Rychlik, et al., 2020). We use the same data set as used in Teixeira Parente et
99 al. (2019), who performed sensitivity analysis using the active subspace of the Kerschbaum
100 spring discharge signal. This allows us to compare the results obtained from the tem-
101 poral scale-dependent sensitivity analysis with those obtained using the entire discharge
102 signal. In Section 2, we provide details about the mathematical framework for coupling
103 the active subspace method with DWT as well as a short description of the model and
104 used data. In Section 3, we explain and discuss the results of the methodology as ap-
105 plied to the illustrative example of the Kerschbaum spring LuKARS model. Finally, we
106 summarize our findings in Section 4.

107 **2 Methodology**

108 The methodology that we present in this work, aims at decomposing both, the mod-
109 eled and the measured discharge signal at different scales using DWT and, hence, to per-
110 form an independent sensitivity analysis for each temporal scale. Then, we test if the

111 dimension and structure of the active subspaces identified, i.e. the sensitive physical pa-
 112 rameters, are different among different scales. This means that we try to identify if dif-
 113 ferent temporal scales of the modeled discharge signal are sensitive to changes in differ-
 114 ent model parameters. If so, we want to investigate if these scales can be approximated
 115 by an active subspace with different dimension and eigenvectors. We apply the proposed
 116 methodology to a real case study, where we use a lumped karst hydrological model, i.e.
 117 LuKARS, to model the discharge of the Kerschbaum spring in Waidhofen a.d. Ybbs (Aus-
 118 tria). This entire process is summarized in Fig. 1. For reproducibility, the codes and data
 119 of the methodology can be downloaded from Bittner, Engel, et al. (2020).

120 **2.1 Coupling DWT with Active Subspaces**

121 In the following, we provide a detailed explanation of how we couple the DWT with
 122 the active subspace method. For convenience, matrices are underlined twice and vectors
 123 once. Scalars and sets are not indicated with an underline. If the output of a function
 124 G of a quantity \bullet is a matrix, it is notated as $\underline{\underline{G}}(\bullet)$. We do this analogously for vectors,
 125 scalars and sets. A quantity, e.g. spring discharge time series, is considered as transformed
 126 if it was decomposed from the original to the wavelet basis. To distinguish between orig-
 127 inal and transformed quantities, $\tilde{\bullet}$ is introduced as the transformed quantity and $\hat{\bullet}$ as
 128 the approximated version of $\tilde{\bullet}$ within the transformed wavelet basis.

129 **2.1.1 Discrete Wavelet Transform**

130 The starting point of this work is to define a hydrological model $G(X)$ and to col-
 131 lect time series data \underline{d} that should be simulated by the model, here the discharge of the
 132 Kerschbaum spring (Step 1 in Fig. 1). Then, the next step is to choose a DWT (Step
 133 2 in Fig. 1), i.e. a mother wavelet, and decompose the measured and simulated discharge
 134 time series into several temporal scales using the DWT. Our measured discharge time
 135 series \underline{d} consists of n data points. The natural frequency of discrete wavelet transforma-
 136 tions is two (Walnut, 2013). Hence, n is chosen as

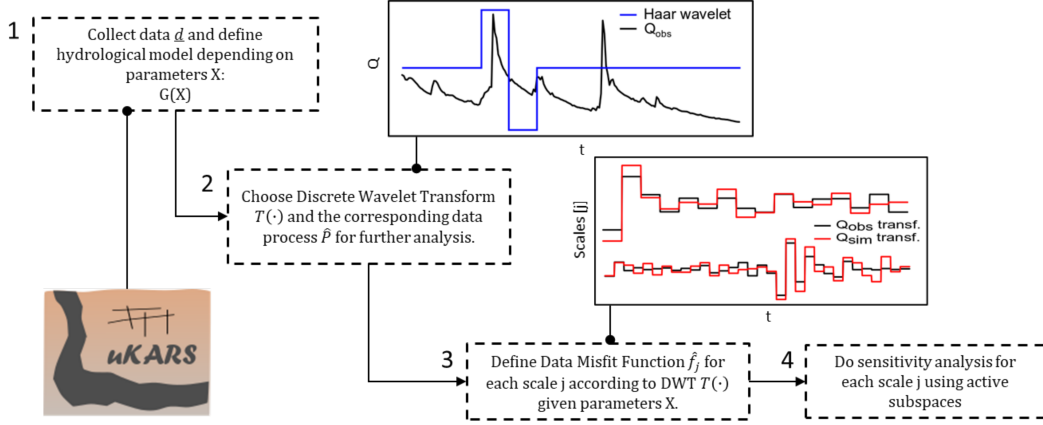


Figure 1. Flowchart of the methodology for coupling the active subspace method with the discrete wavelet transform.

$$n = 2^m, \quad (1)$$

137 where $m \in \mathbb{N}$. A scale j is defined as the details coefficients \tilde{d}_j corresponding to
 138 the $(m-j)$ -th iteration in a filter bank (Mallat, 1989). The filter bank recursively splits
 139 the given time series in the details and approximation coefficients \tilde{a}_j as defined in Walnut
 140 (2013). This means that the details coefficients of scale j are obtained by decomposing
 141 the approximation coefficients of scale $(j + 1)$. In total, we have $(m + 1)$ scales. Ac-
 142 cordingly, we define $T(\bullet)$ as the discrete wavelet transformation of the measured and mod-
 143 eled discharge time series:

$$\tilde{d}_j = T_j(\underline{d}) \quad \forall j = 0 \dots m. \quad (2)$$

144 The transformation T gives a set of details coefficients with m members and one
 145 approximation coefficient \tilde{a}_0 which is referred to as the details coefficient of Scale 0 \tilde{d}_0 .
 146 Hence, the subscript j chooses a member of the set given by T : the scale j of the trans-
 147 formed discharge. Thus, the decomposition of the simulated output from the hydrolog-
 148 ical model G into its temporal scales can be written as

$$\tilde{\underline{G}}_j = T_j(\underline{G}). \quad (3)$$

149 **2.1.2 Definition of the Data Misfit Function for different scales**

150 The decomposition of the measured and modeled discharge time series is the most
 151 important part in our methodology since the sensitivity has to be quantified with respect
 152 to the gradient of a data misfit between measured and simulated discharge for each scale.
 153 Thus, to perform a sensitivity analysis of each scale with respect to the data misfit we
 154 need an evaluation function for each scale. Similar to Teixeira Parente et al. (2019), we
 155 define the Data Misfit Function (DMF) between the measurements \underline{d} and the simulated
 156 discharge $\underline{G}(\underline{X})$ with a set of model parameters \underline{X} as

$$f(\underline{X}) = \frac{1}{2} \|\underline{\Gamma}^{-\frac{1}{2}}((\underline{d} - \mu_t) - (\underline{G}(\underline{X}) - \mu_t))\|_2^2, \quad (4)$$

157 where $\|\bullet\|_2^2$ is the square of the Euclidean norm. Note that the shift μ_t is the av-
 158 erage of \underline{d} with respect to time.

159 The DMF in Eq. 4 corresponds to a Gaussian measurement noise. It can be mod-
 160 eled as a discrete Gaussian Process $GP(\underline{d})$. Such a process is completely defined by its
 161 covariance matrix $\underline{\Gamma}$ and its mean vector which should be equal to the measured data
 162 \underline{d} . Here, $\underline{\Gamma}$ is a diagonal matrix describing an homoscedastic error. In this work, we con-
 163 sider an error on the measured discharge of 2 ls^{-1} . The advantage and the limitations
 164 of this assumption will be discussed later on. So far, we only defined the DMF within
 165 the original basis. Thus, to stay with a Gaussian model, the construction of the DMFs
 166 within the wavelet basis requires the definition of the mean vector \underline{d}_j and covariance ma-
 167 trix $\underline{\Gamma}_j$ for each scale j . It is important to recall that the DMF aims at quantifying the

168 error between model and measured values, considering that the measured values and their
 169 wavelet transform are uncertain.

170 For that reason, we need to ensure that the DWT of the original signal properly
 171 distributes the uncertainty among each scale. As a consequence, coupling the active sub-
 172 space method with DWT requires to transform the random process as a whole in order
 173 to properly define a DMF $\tilde{f}_j(\underline{X})$ for each scale j (Step 3 in Fig. 1). The idea is to find
 174 a mother wavelet (Step 2 in Fig. 1) such that the scales are statistically independent from
 175 each other. By that, we ensure obtaining independent information about the sensitiv-
 176 ity of the parameters from each scale without any loss of information about the uncer-
 177 tainty in the measurements.

178 The term information is used in a Shannon Entropy sense (Shannon, 1948), refer-
 179 ring to the loss of information as the dependence between the scales. As a measure for
 180 this information loss, we introduce the Kullback-Leibler-Divergence of the whole trans-
 181 formed process in the wavelet domain \tilde{P} and the lumped process \hat{P} , in which the scales
 182 are assumed to be independent. We refer to this as the Wavelet Mutual Information (*WMI*),
 183 since the idea is based on the approaches for obtaining the Mutual Information (*MI*)
 184 of random variables as described in Cover and Thomas (2012):

$$WMI(\tilde{P}) := D_{KL}(\tilde{P} \parallel \hat{P}). \quad (5)$$

185 As \tilde{P} and \hat{P} are discrete processes, it is feasible to model them as multivariate Prob-
 186 ability Density Functions. Hence, the *WMI* for a discrete Gaussian scale process \widetilde{GP}
 187 can be obtained by inserting the definition of a multivariate Gaussian into Eq. 5:

$$WMI(\widetilde{GP}(\underline{d})) = \frac{1}{2} \left(\ln \left(\frac{\det \hat{\underline{\Gamma}}}{\det \underline{\Gamma}} \right) + \text{tr}(\hat{\underline{\Gamma}} \underline{\Gamma}^{-1} - \underline{I}) \right), \quad (6)$$

188 where \underline{I} is the identity. If the WMI is equal to 0, we do not lose any information
 189 by assuming independent scales. Accordingly, we look for a transformation T of the Gaus-
 190 sian measurement data \underline{d} with a constant error, such that

$$WMI(T(GP(\underline{d}))) = 0 \quad (7)$$

191 or that the dependence error is as small as possible. Having this transformation
 192 T , we define the new DMF's for each scale \tilde{f}_j with respect to the corresponding random
 193 process \tilde{P}_j . Note that \tilde{f}_j can only be obtained if we did not lose any information. If that
 194 is the case, we obtain statistically independent scales. Otherwise only an approximative
 195 version - assuming independent scales - \hat{f}_j could be used. Since the resulting process of
 196 the transformation of a discrete Gaussian Process is not necessarily Gaussian anymore,
 197 the calculation of the process in the coefficient domain \tilde{P} or the WMI can be compu-
 198 tationally demanding. It is an iterative approach obtaining a suitable wavelet transfor-
 199 mation which maintains all information given by the data. It is possible to demonstrate
 200 (see Appendix A) that the Haar-Wavelet yields that the WMI computes to 0 for homoscedas-
 201 tic Gaussian errors. Nevertheless, it is important to note that for an heteroscedastic er-
 202 ror, e.g. a non-constant diagonal covariance matrix $\underline{\Gamma}$, the WMI might be small but does
 203 not compute to 0. For that reason, we choose a homoscedastic measurement error of 2 ls^{-1}
 204 for the proposed methodology.

205 For the Haar-Wavelet, the set of the new DMFs \hat{f} can be looked at as \tilde{f} , since all
 206 computations are exact and no information is lost. Hence, they can be defined for each
 207 scale j (Step 3 in Fig. 1) as follows:

$$\tilde{f}_j(\underline{X}) = \frac{1}{2} \|\tilde{\underline{\Gamma}}_j^{-\frac{1}{2}} ((\underline{\tilde{d}}_j - \tilde{\mu}_{t_j}) - (\tilde{G}_j(\underline{X}) - \tilde{\mu}_{t_j}))\|_2^2, \quad (8)$$

208 where $\tilde{\underline{\Gamma}}_j$ is the covariance matrix and $\tilde{\mu}_{t_j} = 0$ the mean vector within scale j , whereas
 209 $\tilde{\mu}_{t_0} = \mu_t$.

210 For the Haar-Wavelet the transformed shift $\tilde{\mu}_t$ is equal to 0 for all scales except Scale 0.
 211 For Scale 0, this shift is equal to the quantity of the discharge signal. This follows from
 212 the splitting Lemma as stated in Walnut (2013). Nevertheless, it is not necessary to trans-
 213 form the shift μ_t separately. It was intrinsically transformed by transforming the already
 214 shifted original domain measurement time series and the shifted simulated one:

$$(\underline{\tilde{d}}_j - \tilde{\mu}_{t_j}) := T_j ((\underline{d} - \mu_t)). \quad (9)$$

215 For the Haar-System and our measurement data of length 2^m the shifting was not
 216 necessary but for sake of completeness it shall be done here as the approach shown in
 217 this paper could be adapted onto other basis functions or time series that require such
 218 a shifting due to wavelet boundary effects padding issues. In fact, the approach shown
 219 in this paper can be done for every basis function that supports a decomposition as given
 220 in Eq. 2.

221 **2.1.3 Active Subspaces for Sensitivity Analysis within Different Scales**

222 Having \tilde{f} and \tilde{G} we conduct the sensitivity analysis using the Active Subspace method
 223 exactly as in Teixeira Parente et al. (2019). The only difference is that this is done for
 224 the m corresponding decomposed DMFs and model outputs as input (Step 4 in Fig. 1).
 225 Accordingly, the Active Subspace method gives the eigenvectors $\underline{v}_{j,k}$ of a gradient ma-
 226 trix \underline{C}_j for each scale j defined as follows:

$$\underline{C}_j = E[\nabla_X \tilde{f}_j(\underline{X}) \nabla_X \tilde{f}_j(\underline{X})^T] = \underline{W}_j \underline{\Lambda}_j \underline{W}_j^T, \quad (10)$$

227 where $\underline{W}_j = [\underline{v}_{j,1} \dots \underline{v}_{j,n}]$ and $\underline{\Lambda}_j = \text{diag}(\lambda_{j,1} \dots \lambda_{j,n})$ having $\lambda_{j,k} \geq \lambda_{j,k+1}$. The
 228 first index j is the scale and the second denotes the eigenvector k .

229 Thus, the eigenvalues $\lambda_{j,k}$ are a measure for the sensitivity of the scale DMF \tilde{f}_j with
 230 respect to the corresponding eigenvectors $\underline{v}_{j,k}$. Note that the eigenvectors form an or-
 231 thonormal basis. They contain those linear combinations of input parameters which are
 232 most informed by the measured discharge data within scale j . Informed means that the
 233 objective function $\tilde{f}_j(\underline{X})$, measuring the deviation from observed data within scale j , is
 234 sensitive to this linear combination of parameters.

235 The scale sensitivity score $s_{j,i}$ of parameter x_i within scale j is calculated by

$$s_{j,i} = \sum_{k=1}^K \lambda_{j,k} v_{j,k,i}, \quad (11)$$

236 where K is the number of parameters and i denotes the parameter. Note that $s_{j,i}$
 237 is not the global total sensitivity, where global means that the sensitivity is measured
 238 when varying all parameters simultaneously. It is solely global within scale j . For ac-

239 cessing the global total measure, a weighting of the gradient of the scale DMF with re-
240 spect to its contribution to the gradient of the total DMF would be necessary. However,
241 no weighting is considered in this work since our intention is to use the entire signal of
242 the discharge for the wavelet decomposition to obtain an independent information for
243 each time scale.

244 **2.2 Kerschbaum spring LuKARS model**

245 The Kerschbaum springshed is located close to the city of Waidhofen a.d. Ybbs in
246 Austria Fig. 2. The recharge area of the mainly dolomitic karst system covers about 2.5 km²
247 and can, thus, be considered as a small scale, pre-alpine catchment. Despite the small
248 spatial scale of the recharge area, the Kerschbaum spring represents the major source
249 of freshwater supply for the region. Fig. 3 classifies the behavior of the Kerschbaum spring
250 by means of statistical and spectral indices. The cross-correlation between precipitation
251 and spring discharge, shown in Fig. 3a, highlights a quick response to precipitation events
252 after 1 day with the highest correlation coefficient r_{xy} of 0.37. Moreover, we can iden-
253 tify a quick decrease of r_{xy} , pointing towards a rapid propagation of the input signal (pre-
254 cipitation) through the aquifer (Labat et al., 2000a; Mangin, 1984). In the cross-correlation
255 as well as in the spectral density (Fig. 3b), we can identify a sudden change in slope from
256 2.35 to 1.32 after 8 days. This change points towards an activation of drainage from the
257 aquifer storage, i.e. baseflow (Larocque et al., 1998). More information about the study
258 site are given in Bittner et al. (2018) and Narany et al. (2019).

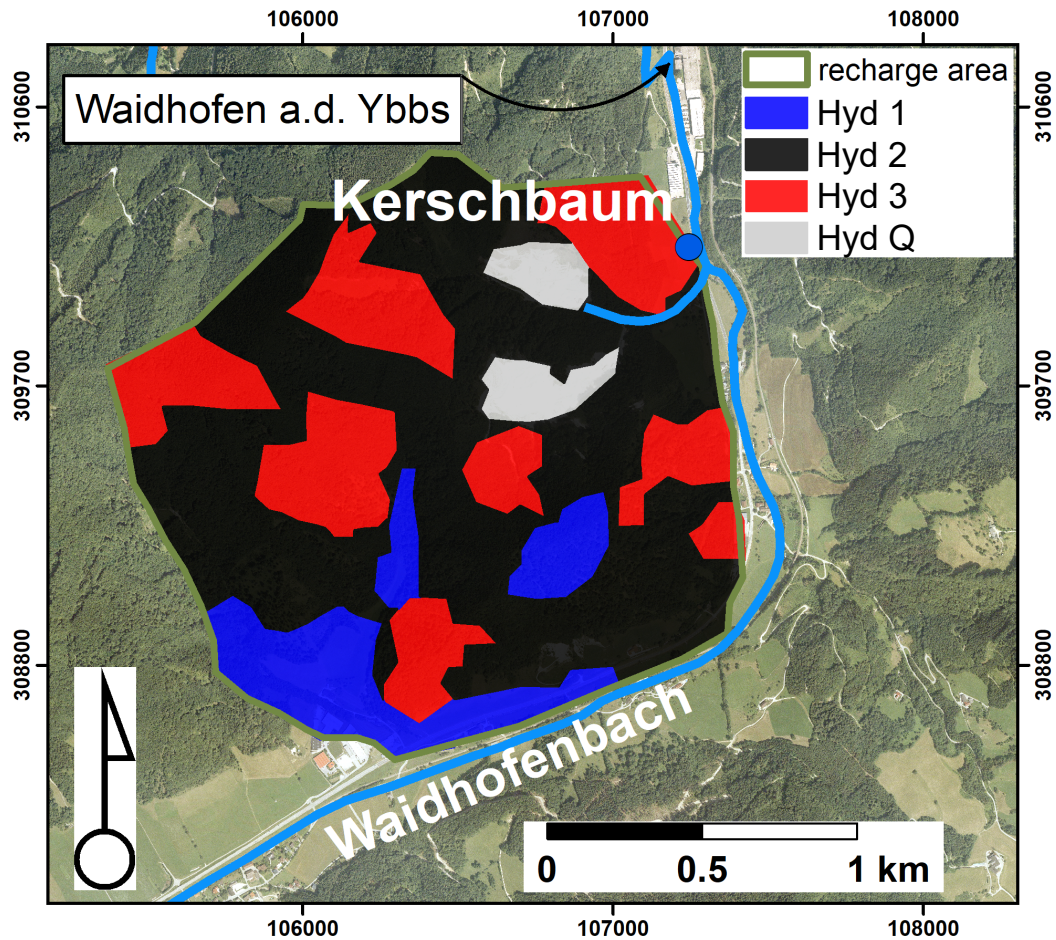


Figure 2. Recharge area of the Kerschbaum spring close to waidhofen a.d. Ybbs (Austria) including the distribution of hydrotopes, i.e. Hyd 1 (13 % of recharge area), Hyd 2 (56 % of recharge area), Hyd 3 (27 % of recharge area) and Hyd Q (4 % of recharge area). The orthophoto was kindly provided by the waterworks owner in Waidhofen a.d. Ybbs.

259 The LuKARS model was developed by (Bittner et al., 2018) to investigate how min-
 260 ing activities in the recharge area affect the quantity of discharge in the Kerschbaum spring.
 261 A GUI for the model is available as open source plugin for FREEWAT (Rossetto et al.,
 262 2018) in QGIS (Bittner, Rychlik, et al., 2020). The model is based on the implementa-
 263 tion of hydrotopes, i.e. areas with homogeneous soil and land use characteristics (Arnold
 264 et al., 1998), shown in Fig. 2. Determined by its individual physical characteristics, each
 265 hydrotope shows a distinct response to an input event, e.g. precipitation or snow melt.
 266 All hydrotopes simulate three types of flow, i.e. quickflow through conduits, groundwa-
 267 ter recharge and secondary spring discharge. They all share one common baseflow stor-

age, i.e. the saturated zone, to which the recharge is transferred. The sum of all hydro-
tope quickflow responses at a given time step represents the conduit flow in the recharge
area. Then, the sum of the integrated hydrotope quickflows and the baseflow simulate
the spring discharge. The equations of the LuKARS model are provided in Appendix
B. The model parameter ranges used in this study are shown in Table 1. Further, we
use daily data for precipitation, temperature, snow depth and spring discharge in the pe-
riod from January 2006 to December 2008 to run the model. It is important to note that,
in order to apply the active subspace method, all model parameters need to be indepen-
dent from a statistical point of view. However, in LuKARS the parameters of one hy-
drotope are dependent on the parameters of other hydrotopes, as shown in Eq. C1 of Ap-
pendix C. Therefore, we follow the framework proposed for the Kerschbaum LuKARS
model in Teixeira Parente et al. (2019). For the seek of completeness, we include this method-
ology in Appendix C. Since this transformation does not have an impact on the inter-
pretation of the results shown in the following section, it will not be further discussed.

Table 1. Overview of the model parameter ranges defined for all hydrotopes. The respective numbers indicate the lower bound and the upper bound of the parameter ranges used as prior intervals. For the meaning of the parameters, we refer to the explanation given in Appendix B.

Hydrotope	k_{hyd} [m ² d ⁻¹]	E_{min} [mm]	E_{max} [mm]	α [-]	k_{is} [m mm ⁻¹ d ⁻¹]	k_{sec} [m mm ⁻¹ d ⁻¹]	E_{sec} [mm]
Description	discharge coef. quickflow	min. storage capacity	max. storage capacity	quickflow exponent	discharge coef. recharge	discharge coef. sec. springs	activation level sec. springs
Hyd 1	9 - 900	10 - 50	15 - 75	0.7 - 1.6	0.002 - 0.2	0.0095 - 0.95	25 - 70
Hyd 2	8.5 - 850	40 - 80	80 - 160	0.5 - 1.3	0.00055 - 0.055	0.0023 - 0.23	130 - 220
Hyd 3	7.7 - 770	75 - 120	155 - 255	0.2 - 0.7	0.00025 - 0.025	0.0015 - 0.15	320 - 450

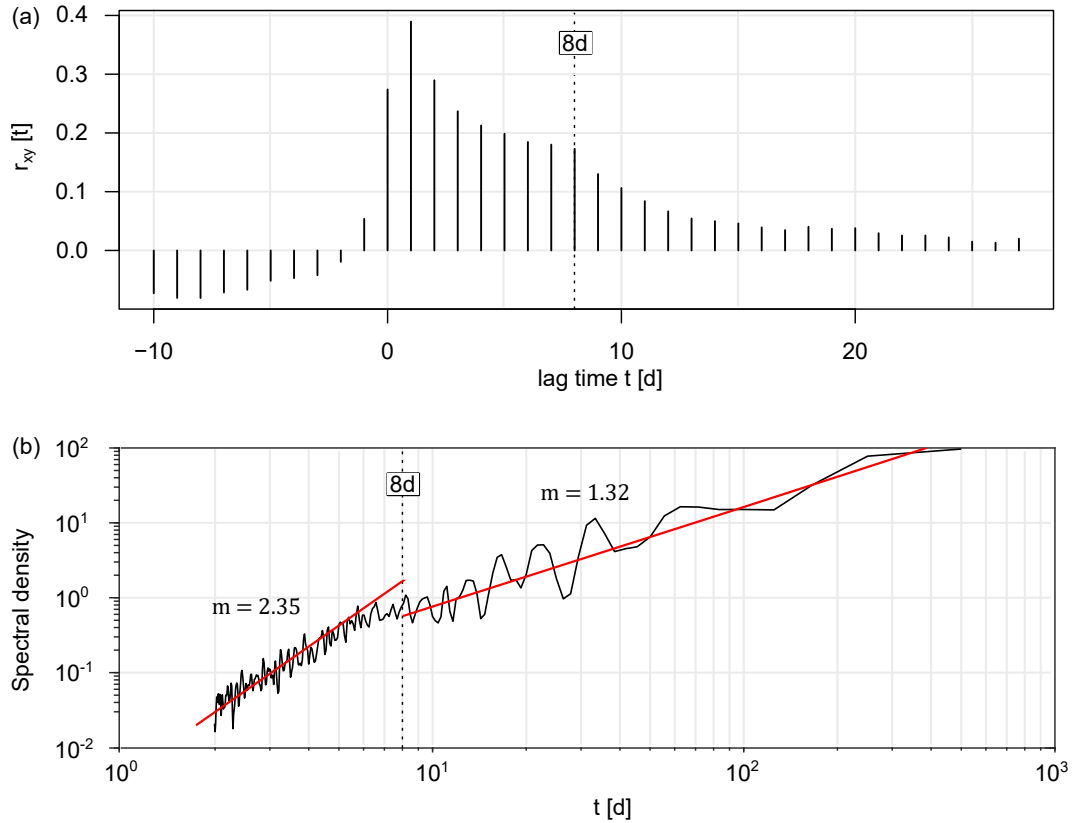


Figure 3. Time series analysis of the Kerschbaum spring discharge. a) The cross-correlation between precipitation and the spring discharge, highlighting a quick response of 1 day lag time and storage effects after 8 days. b) The spectral density of the discharge signal, also highlighting an abrupt change in spectral density of variance after 8 days, indicated by a change in slope from $m = 2.35$ to $m = 1.32$.

282 3 Results and discussion

283 In the following section, we describe and discuss the results related to the appli-
 284 cation of our methodology to the Kerschbaum LuKARS model. In detail, we discuss the
 285 dimensions of active subspaces on different scales, the scale features of the different eigen-
 286 vectors as well as the hydrological meaning of identified scale dependencies. In the fol-
 287 lowing, the order of scales is from the lowest to the highest frequency. To be precise, Scale 1
 288 represents the lowest frequency, i.e. 1024 days, and Scale 10 the highest frequency, i.e.
 289 2 days. Finally, Scale 0 represents the mean of the discharge signal.

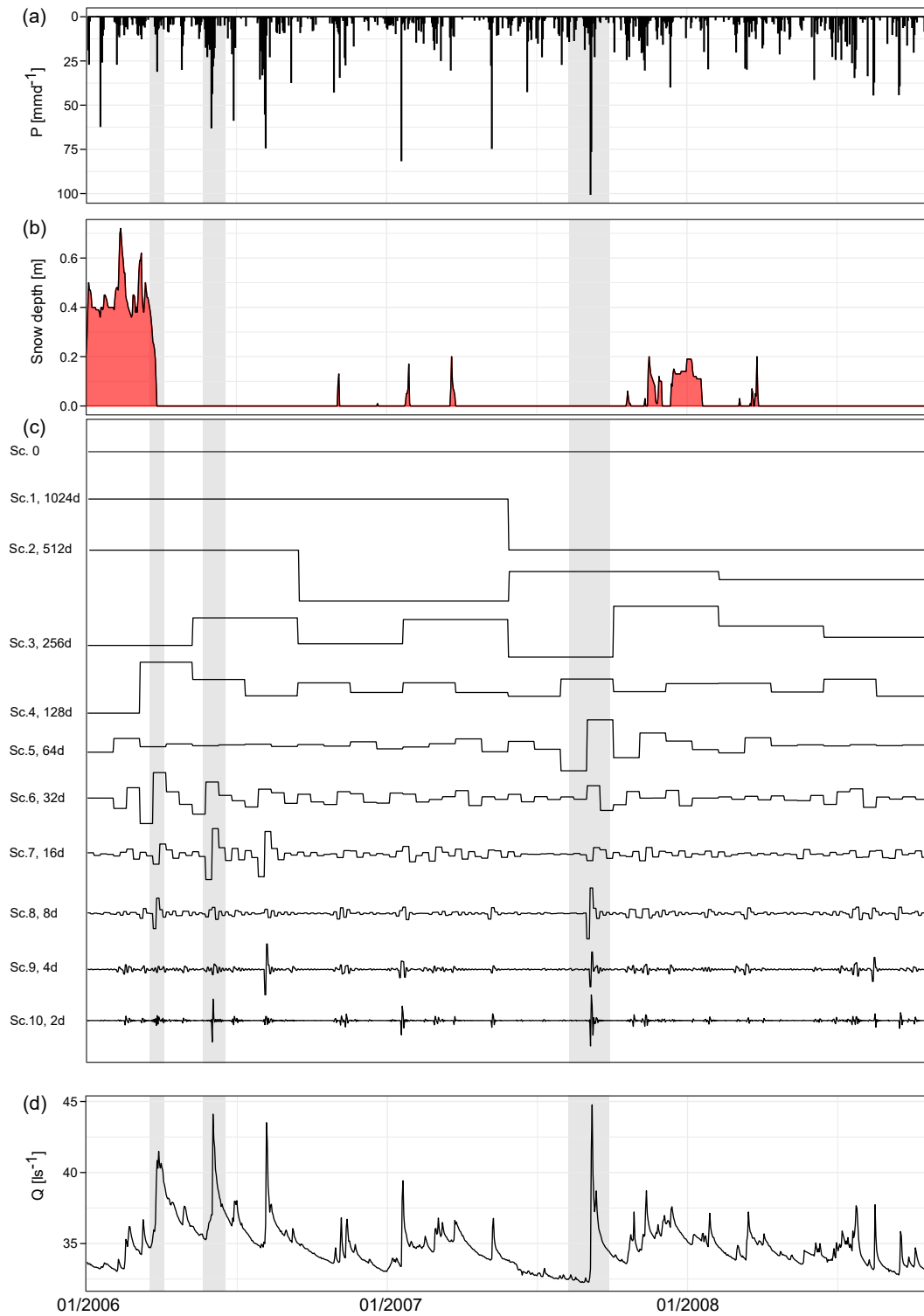


Figure 4. Data time series used in the LukARS model for the period of interest from 2006 to 2008 and the discrete wavelet scales of the measured discharge time series. a) Precipitation, b) measured snow depths, c) the discrete wavelet scales (Sc.) of the Kerschbaum spring discharge signal and d) the Kerschbaum spring discharge time series. The grey bars highlight specific peak flow events during the period of interest. Note that Scale 10 represents the highest frequency, i.e. 2 days, whereas Scale 1 represents the lowest frequency, i.e. 1024 days.

290 Fig. 4 shows how precipitation (Fig. 4a) and snow melt (Fig. 4b) affect the discrete
 291 wavelet scales of the Kerschbaum spring discharge (Fig. 4c) as well as the complete dis-
 292 charge signal (Fig. 4d). Notice that Fig. 4c does not display the values on the y-axis be-
 293 cause they are not relevant for the following qualitative interpretation. As an example,
 294 we highlight three significant peak discharges with grey colored frames in the background.
 295 These fast spring discharges happened in response to major snow melt, e.g. April 26th,
 296 2006, or precipitations events, e.g. June 2nd, 2006. In the DWT scales (Fig. 4c), we can
 297 observe that major input events have an effect on the spring discharge from 2 days up
 298 to a period of 8 days, which is similar to what we identified in the cross-correlation and
 299 spectral analysis (Fig. 3). Very intense input events, such as the precipitation event on
 300 September 6th, 2007, can affect even more temporal scales, up to 64 days. This is con-
 301 sistent for example with the observations of Schaeffli et al. (2007) and other works in the
 302 literature (Charlier et al., 2015; Yang et al., 2012) and shows that when we decompose
 303 the hydrologic signal among multiple temporal scales, high flow conditions have an im-
 304 pact on scales larger than the event duration.

305 3.1 Scale dependence of active subspaces

306 Fig. 5a shows the decay of the eigenvalues of each wavelet scale over the first 9 eigen-
 307 values and the truncation level. Based on our findings from the cross-correlation, spec-
 308 tral analysis and the DWT, we can distinguish between two groups of scales highlighted
 309 in Fig. 5a and b. Group 1 represents the sub-monthly to superannual scales, i.e. Scale 1
 310 to Scale 7. Group 2 represents the sub-weekly to weekly, i.e. Scale 8 to Scale 10. The
 311 lower frequencies (Group 1) have active subspace dimensions between 2 and 3. In com-
 312 parison, the sub-weekly to weekly scales (Group 2), representing faster spring discharge
 313 responses (Fig. 4c), only have active subspace dimensions between 1 and 2. We decided
 314 to truncate an active subspace after an eigenvalue decay over one order of magnitude.
 315 This choice, although arbitrary, does not affect the main outcomes of the analysis as dis-
 316 cussed by Teixeira Parente et al. (2019). The eigenvalues are normalized to the maxi-

317 mum eigenvalue of each scale to allow for a comparability of the decays between each
 318 scale. When looking at the eigenvalue decay of each scale (Fig. 5a), we can identify that
 319 Scale 0 shows the weakest decay of all scales. Moreover, we find that with an increas-
 320 ing wavelet scale, the eigenvalues decay faster. The dimension of the active subspaces
 321 identified for both Group 1 and Group 2 are lower as compared to the original active sub-
 322 space of the Kerschbaum LuKARS model computed without the DWT, i.e. 4 (also shown
 323 in Fig. 5b). The fact that each wavelet scale has a low dimensional active subspace in-
 324 dicates that fewer eigenvectors are sensitive and informed.

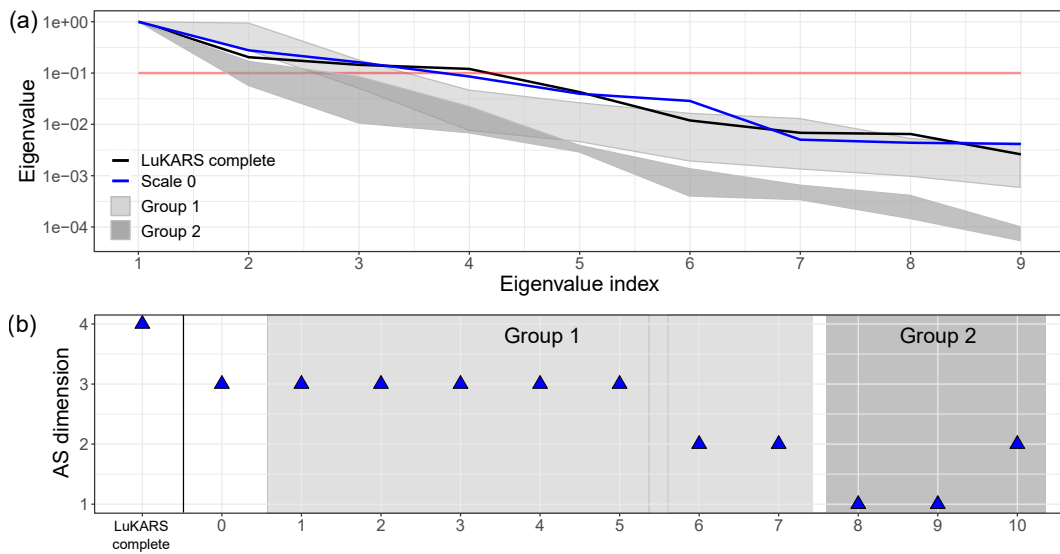


Figure 5. Active subspace dimensions. a) Eigenvalue decay of both scale groups, i.e. Group 1 representing Scale 1 to 7 and Group 2 representing Scale 8 to 10, Scale 0 and 'LuKARS complete' normalized to the maximum eigenvalue of each scale. The horizontal red line indicates the truncation level above which the active subspace is defined. b) Active subspace dimension of each discrete wavelet scale grouped in both groups of scales. 'LuKARS complete' shows the active subspace dimension when applying the active subspace method to the Kerschbaum LuKARS model without the DWT.

325 3.2 Eigenvector features on different scales

326 In Fig. 6, we show the first three eigenvectors of the complete LuKARS model (Bittner
 327 et al., 2018) and one representative scale for each group, i.e. Scale 1 for Group 1 and Scale 8
 328 for Group 2. In the relevant eigenvectors of the complete LuKARS model (Fig. 6a), we

329 can observe a strong contribution of the discharge coefficient of groundwater recharge
 330 from each hydrotope, i.e. k_{is} . Moreover, we see that Hyd 2 has the highest contribution,
 331 which is the largest hydrotope in the recharge area (see Fig. 2). The second highest con-
 332 tribution comes from Hyd 1, representing the most dynamic hydrotope in terms of dis-
 333 charge variability. Although the area of Hyd 3 is larger than Hyd 1 (Fig. 2), its contri-
 334 bution to the first eigenvector is weakest. When further taking into account Eigenvec-
 335 tors 2 and 3, a similar pattern in terms of contributing hydrotopes can be observed, i.e.
 336 Hyd 1 and Hyd 2 are dominant. It can be seen that k_{hyd} of Hyd 1 and 2, which are the
 337 discharge coefficients of the quickflow, have noticeable scores in Eigenvector 2, .

338 Looking at the first eigenvector of Scale 0 (Fig. 6b), we also find that mainly the
 339 groundwater recharge parameters (k_{is}) of each hydrotope have the highest contribution
 340 in the first eigenvector. Moreover, we can observe the same ranking of hydrotope con-
 341 tributions in the first eigenvector compared to the complete LuKARS model, i.e. in de-
 342 creasing order Hyd 2, Hyd 1 and Hyd 3. When further taking into account Eigenvector 2
 343 and 3, we further notice high scores of the quickflow parameters k_{hyd} of Hyd 1 and Hyd 2.

344 Next, we look at the eigenvectors of Scale 1, being representative for the scales of
 345 Group 1. In all eigenvectors (Fig. 6c), we can observe a dominant contribution of Hyd 1
 346 and Hyd 2 parameters, similar to Scale 0. In contrast to Scale 0, Hyd 1 parameters show
 347 a higher contribution as compared to those of Hyd 2. When looking at single parame-
 348 ter contributions in each eigenvector, we generally observe highest scores of the discharge
 349 coefficients of k_{is} and k_{hyd} of Hyd 1 and Hyd 2. Moreover, the water storage thresholds,
 350 i.e. E_{min} and ΔE (in the following referred to as the E parameters), of both dominant
 351 hydrotopes have noticeable contributions in the eigenvectors. These parameters control
 352 the onset and offset of the quickflow and, thus, further control the amount of water be-
 353 coming groundwater recharge.

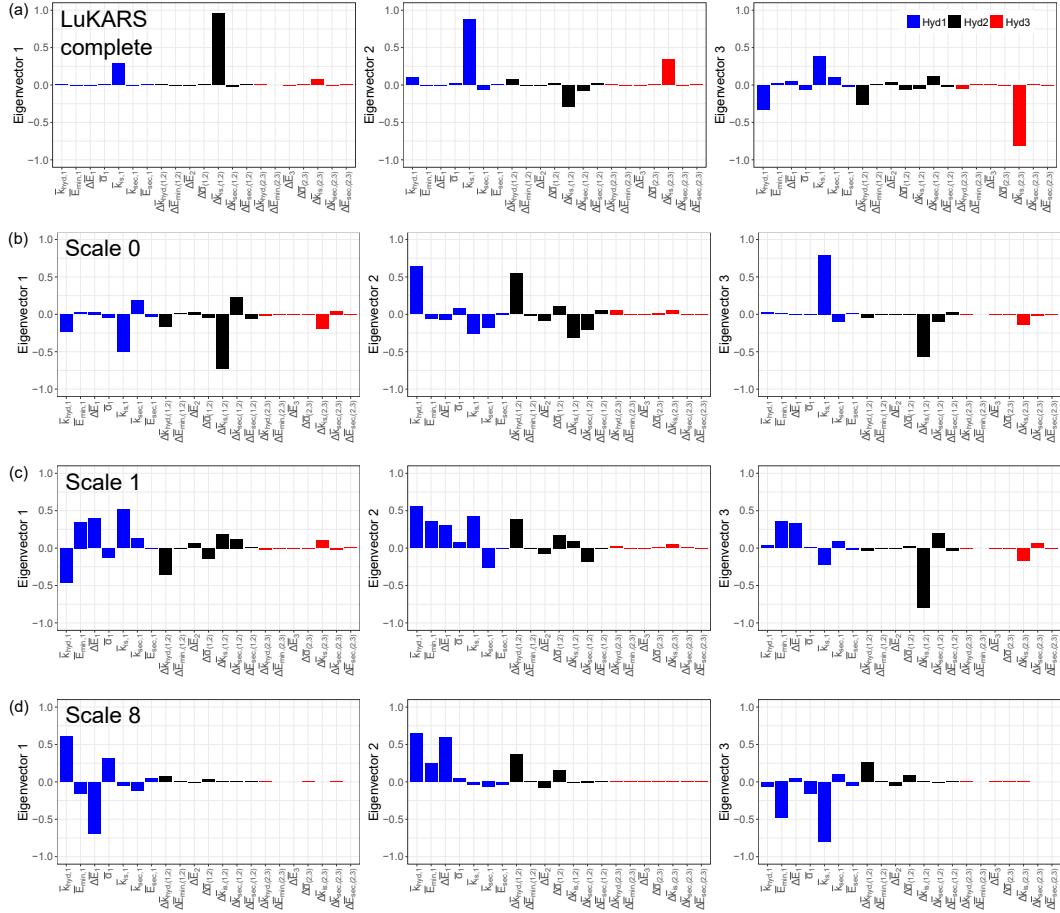


Figure 6. First three eigenvectors of Scale 0, 1 and 8. 'LuKARS complete' are the eigenvectors computed without scale dependencies.

354 Although we are showing the first three eigenvectors of Scale 8 (Fig. 6d), only the
 355 first eigenvector is relevant as highlighted by the active subspace dimensions in Fig. 5b.
 356 Looking at the parameters contributing to the relevant eigenvector, we notice a clear dom-
 357 inance of Hyd 1 parameters and negelectable scores of both other hydrotopes. In par-
 358 ticular, k_{hyd} , the E parameters and α have the highest scores. These parameters primar-
 359 ily control the quickflow of Hyd 1, where α regulates the magnitude of quickflow events.
 360 In contrast to the previously discussed scales, no significant contribution from ground-
 361 water recharge controlling parameters can be noticed. These results are in a good agree-
 362 ment with the identified impacts of snow melt and precipitation events on the tempo-
 363 ral scales of the spring discharge. As Hyd 1 has the highest quickflow variability, this hy-

364 drotope contributes most to the peakflow during these events, which explains the high
 365 importance of the quickflow parameters in Group 2 scales.

366 3.3 Scale-dependent parameter sensitivities

367 Next, we show the parameter sensitivities for each wavelet scale and the complete
 368 LuKARS model in Fig. 7a. Both, Scale 0 and the complete LuKARS model without scale
 369 dependencies have a similar pattern in terms of sensitive parameters, comparable to our
 370 findings in the eigenvectors of the dominant eigenvalues (Fig 6a and b). In particular the
 371 k_{is} parameters of each hydrotope are the most sensitive parameters with decreasing scores
 372 from Hyd 2 over Hyd 1 to Hyd 3. Looking at the sensitive parameters on the sub-monthly
 373 to superannual scales (Group 1), we can observe that Hyd 1 parameters are most sen-
 374 sitive in all scales. Moreover, k_{is} is the most sensitive parameter of Hyd 2 with notice-
 375 able scores in all scales of Group 1. For Hyd 3, k_{is} is only sensitive in Scale 1 and 2. In
 376 general, the most sensitive parameters in the sub-monthly to superannual scales are the
 377 discharge coefficients of the quickflow, i.e. k_{hyd} , and the recharge, i.e. k_{is} . Focussing on
 378 the parameter sensitivities of the sub-weekly to weekly scales (Group 2), no noticeable
 379 scores can be found in Hyd 2 and Hyd 3, with the only exception given by k_{hyd} and k_{is}
 380 of Hyd 2 in Scale 7. All sensitive parameters on these scales are related to Hyd 1, which
 381 are particularly those controlling the quickflow, i.e. k_{hyd} , the E parameters and α .

382 Fig. 7b shows the total number of sensitive parameters cumulated over all discrete
 383 wavelet scales. We start cumulating sensitive parameters at Scale 10, since it has the high-
 384 est frequency and represents the quickest response of the decomposed discharge signal.
 385 We consider a parameter to be sensitive if its score is larger than 0.01. This value in-
 386 dicates the 0.75-quantile of all sensitivity scores computed for each scale. Parameters which
 387 are sensitive on more than one scale are counted only once in the scale of its first appear-
 388 ance. We observe that a total of 11 parameters are sensitive over all scales. In compar-
 389 ison, in the complete LuKARS model without scale dependencies, only 7 parameters are
 390 sensitive. This shows that further information about sensitive parameter can be hidden

391 in the temporal scales of the discharge. From a physical point of view, this can be ex-
392 plained by the temporal-scale dependent relevance of different hydrologic processes, for
393 which different model parameters can be sensitive.

394 **3.4 Hydrological interpretation**

395 In general, we found the weakest eigenvector decay for Scale 0 and decreasing active
396 subspace dimensions with increasing wavelet scales. As introduced in Section 2.1,
397 Scale 0 represents the mean of the discharge signal. From a physical point of view, the
398 mean of the spring discharge signal represents an interplay of multiple hydrological pro-
399 cesses, which are represented in LuKARS as quickflow and baseflow. Thus, to reproduce
400 the mean of the discharge signal, the model also needs to consider both processes. This
401 relevance of different hydrological processes can explain that a larger dimension of the
402 active subspace is needed to sufficiently inform the data misfit function for the mean of
403 the discharge signal. For faster spring responses, i.e. the sub-weekly to weekly scale, we
404 found lower dimensional active subspaces as compared to the sub-monthly to superan-
405 nual scales. This finding is congruent with the results obtained by Bittner, Teixeira Par-
406 ente, et al. (2020). In their synthetic test cases, they showed that spring discharge dom-
407 inated by a single hydrological process displays a low dimensional active subspace (di-
408 mension between 1 and 2). However, here we did not identify such a dependence for hy-
409 pothetical scenarios, but for specific temporal scales of a real spring discharge. Thus, our
410 results highlight that the coupling between DWT and active subspaces supports iden-
411 tifying those temporal scales of a spring discharge for which only a small number of eigen-
412 vectors are sensitive, e.g. 1 as in Scale 8. These high-frequency scales, i.e. the scales of
413 Group 2, are mainly controlled by one dominant hydrological process, e.g. the quickflow
414 from Hyd 1. Further, the coupled methodology allows to identify those temporal scales
415 which are controlled by different hydrological processes, e.g. quickflow and groundwa-
416 ter recharge in Scale 8. For these scales, we found higher dimensional active subspaces,
417 e.g. 3 dimensions for Scale 1.

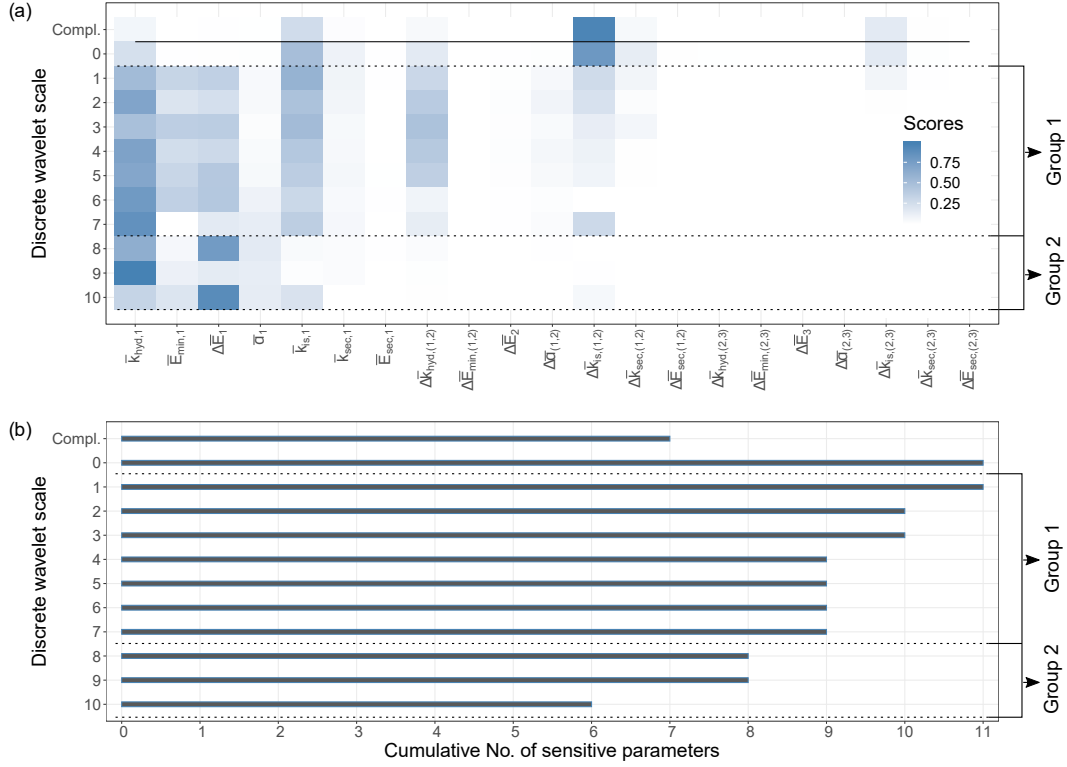


Figure 7. Scale-dependent sensitivities. a) Global sensitivities shown for each model parameter and each scale. The 'Compl' parameter sensitivities represent the sensitivity scores without scale dependencies. b) Cumulative number of sensitive parameters.

418 The dominant parameter contributions in Scale 0, i.e. the recharge coefficient of
 419 Hyd 2, 1 and 3 (k_{is} , Fig. 6b and Fig. 7a), are similar to those found in the dominant eigen-
 420 vectors of the complete discharge signal (Teixeira Parente et al., 2019). As the major vol-
 421 ume of the Kerschbaum spring discharge originates from baseflow (Bittner, Rychlik, et
 422 al., 2020), we argue that this is the reason why those parameters controlling the mod-
 423 eled baseflow, i.e. k_{is} of each hydrotope, are most sensitive in Scale 0. Moreover, k_{is} of
 424 Hyd 2 is most sensitive since Hyd 2 is the largest hydrotope in the area and contributes
 425 most to the groundwater recharge. The noticeable scores of the quickflow parameters k_{hyd}
 426 in Scale 0 highlight that the mean of the discharge signal is composed of baseflow and
 427 quickflow contributions. In general, these findings highlight that the parameters in the
 428 dominant eigenvectors reflect the hydrological processes involved in producing the sig-
 429 nal of a respective scale, here Scale 0.

430 In the scales of Group 1, the discharge coefficients of the groundwater recharge and
431 quickflow (k_{is} and k_{hyd}) of Hyd 1 and Hyd 2 are most sensitive (Fig. 6c and Fig. 7a). As
432 Hyd 1 is the smallest hydrotope, this finding suggests that also on the low-frequency scales
433 of Group 1, the discharge variability of a hydrotope can play a more significant role than
434 the size of a hydrotope. Taking further into account that the storage parameters of Hyd 1
435 and Hyd 2 (E) play an important role in Scale 1, we argue that on the sub-monthly to
436 superannual scales, both hydrological processes, the quickflow and groundwater recharge
437 becoming baseflow, are relevant. Similar to the findings of Schaeffli et al. (2007), we can
438 observe that some discharge peaks, caused by quickflow events in response to intense pre-
439 cipitation or snow melt, also affect higher periods, in our case the scales of Group 1 (Fig. 4c).

440 For scales of Group 2, we notice a clear dominance of quickflow controlling param-
441 eters, in particular the quickflow coefficient (k_{hyd}), the storage parameters (E) and the
442 quickflow exponent (α), in the relevant eigenvector. This shows that on the sub-weekly
443 to weekly scales, groundwater recharge and, thus, the baseflow does not play a signif-
444 icant role. This interpretation is further confirmed by the cross-correlation analysis, which
445 highlighted a dominant contribution from quickflow up to a period of 8 days (Fig. 3a).
446 Hence, our methodology shows that it is possible to identify those hydrological processes
447 which are relevant for a respective temporal scale in the parameters of the relevant eigen-
448 vectors.

449 Finally, we can summarize that for Scale 0 and the sub-monthly to superannual
450 scales, higher dimensional active subspaces are needed to reproduce the signals of these
451 scales. This is due to the fact that different hydrological processes, e.g. the quickflow and
452 the recharge becoming baseflow, from different areas in a catchment, i.e. hydrotopes, are
453 relevant on these temporal scales. These relevant hydrological processes are reflected by
454 the parameters contributing to each dimension of an active subspace, i.e. the eigenvectors
455 of the dominant eigenvalues. On the contrary, only small dimensional active sub-
456 spaces are needed to reproduce the signals on the sub-weekly to weekly scales. This is

457 related to the fact that only the quickflow from the hydrotope with high discharge vari-
458 abilities, i.e. Hyd 1, matters on that temporal scale. These findings lead us to the con-
459 clusion that, for our specific case of the LukARS model, the less complex the hydrologic
460 process structure is on a considered scale, the lower the dimensionality of the related ac-
461 tive subspace. Thus, it is possible to identify dominant hydrological processes for dif-
462 ferent temporal scales in the dimensions of an active subspace. Moreover, our findings
463 show that the time-scale dependence of hydrological processes, represented by the LuKARS
464 model parameters, affects the structure of an active subspace. Furthermore, our find-
465 ings in the scale-dependent parameter sensitivities are similar to what we identified in
466 the eigenvectors of the dominant eigenvalues shown in Fig. 7a. It is interesting to ob-
467 serve that with an increasing scale, i.e. higher frequencies, the sensitivity of the recharge
468 coefficients k_{is} decreases. At the same time, the sensitivity of the quickflow exponent α
469 increases. This result indicates a clear shift in the dominant hydrological processes oc-
470 ccurring on the respective scales, since α is the parameter that controls the intensity on
471 which a quickflow occurs. Generally, our results of the scale-dependent parameter sen-
472 sitivities support the hypothesis that parameters identified for each signal can be directly
473 related to the hydrological processes occurring on these temporal scales.

474 The proposed methodology allows to discover hidden sensitive parameters in the
475 spring discharge. To be precise, we found 11 sensitive parameters when decomposing the
476 discharge signal, whereas only 7 were found with the complete LuKARS model (Fig. 7b).
477 These sensitive parameters are hidden as long as the measured discharge signal is not de-
478 composed. We show that multi-objective calibration, aiming at identifying sensitive pa-
479 rameters for various hydrological processes and requiring different sets of observations,
480 is not the only way to better inform model parameters. Instead, we highlight that it is
481 possible to obtain more information about sensitive model parameters by using only one
482 single data time series, here spring discharge.

483 **4 Summary**

484 In the presented work, we coupled the active subspace method with the discrete
485 wavelet transform. By that, we investigated the temporal scale dependencies of param-
486 eter sensitivities of a lumped karst aquifer model, LuKARS. Here, we did not give weights
487 to the different wavelet scales, but use the entire signal of the discharge for the wavelet
488 decomposition, such that each decomposed signal provides an independent information
489 for the respective time scale. However, a weighting procedure can be useful if we want
490 to favor specific hydrological conditions in model calibration. Moreover, providing a weight
491 for each scale can help to reduce the risk of model overfitting in the solution of an in-
492 verse problem.

493 Although we are aware that measurement errors of hydrological time series are mostly
494 heteroscedastic, we chose a homoscedastic error of 2 ls^{-1} for our measurement such that
495 the WMI computes to 0. By that, we ensure not having any loss of information when
496 decomposing our time series in the wavelet domain. Future works should focus on min-
497 imizing the loss of information when using a heteroscedastic error to account for more
498 realistic measurement error models. This requires a normalized version of the WMI.

499 With the proposed methodology, we showed that the structure of an active sub-
500 space depends on the temporal scale for which it was identified. In particular, we iden-
501 tified two to three dimensional active subspaces for sub-monthly to superannual tempo-
502 ral scales and only one to two dimensional active subspaces for the sub-weekly to weekly
503 scales. This shows that the more hydrological processes are relevant for one particular
504 scale, the higher the dimensionality of an active subspace. For the sub-monthly to su-
505 perannual temporal scales, we found that the parameters controlling the slow flowing ground-
506 water recharge and quickflow are most important. For the sub-weekly to weekly scales,
507 the most sensitive parameters are solely related to the quickflow of one hydrotope. Thus,
508 the relevant linear combinations of parameters of an active subspace translate into the dom-
509 inant hydrological processes for each temporal scale. Moreover, the dimensionality of an

510 active subspace provides a measure for the complexity of hydrologic process structure
 511 on a given temporal scale.

512 Finally, we were able to show that within the proposed methodology, it is possi-
 513 ble to identify parameter sensitivities which are hidden in the temporal scales of a mea-
 514 sured discharge signal. Hence, we do not necessarily need multiple data time series to
 515 identify more sensitive parameters in a multi-objective calibration approach. Instead,
 516 we can also obtain more information about parameter sensitivities from one single, de-
 517 composed time series.

518 **Appendix A Haar Wavelet**

519 In the following, we show how the decomposition using the Haar-Wavelet is done
 520 maintaining all information from the measured data. The transformation correspond-
 521 ing to the details \tilde{d}_{j-1} and approximation coefficients \tilde{a}_{j-1} of a time series \underline{d} can be writ-
 522 ten as a linear transform:

$$\begin{bmatrix} \tilde{a}_j \\ \tilde{d}_j \end{bmatrix} = \begin{bmatrix} \underline{H}(j) \\ \underline{G}(j) \end{bmatrix} \tilde{a}_{j+1}, \quad (\text{A1})$$

$$\underline{H}(j) = \frac{1}{\sqrt{2}} \begin{bmatrix} 1 & 1 & 0 & \dots & 0 \\ 0 & 0 & 1 & 1 & 0 & \dots & 0 \\ & & & \vdots & & & \\ 0 & \dots & 0 & 1 & 1 \end{bmatrix}, \quad j = 1 \dots m, \quad (\text{A2})$$

$$\underline{\underline{G}}(j) = \frac{1}{\sqrt{2}} \begin{bmatrix} 1 & -1 & 0 & \cdots & 0 \\ 0 & 0 & 1 & -1 & 0 & \cdots & 0 \\ & & & \vdots & & & \\ 0 & \cdots & & 0 & 1 & -1 \end{bmatrix}, \quad j = 1 \dots m, \quad (\text{A3})$$

523 where the approximation matrix $\underline{\underline{H}}(j)$ and the details matrix $\underline{\underline{G}}(j)$ are real $[2^{j-1} \times 2^j]$
 524 matrices. For implementation details of $\underline{\underline{H}}(j)$ and $\underline{\underline{G}}(j)$, we refer to Ryan et al. (2019).
 525 Recall that \tilde{a}_1 shall be referred to as the Scale 0 details coefficients \tilde{d}_0 , whereas the ap-
 526 proximation \tilde{a}_0 and, hence, $\underline{\underline{H}}(0)$ is not existing. Accordingly we define:

$$\underline{\underline{G}}(0) = \underline{\underline{1}} \in \mathbb{R}^{1 \times 1}. \quad (\text{A4})$$

527 As the approximation coefficients in the Haar-System always give the energy pre-
 528 serving average within the corresponding interval for a scale j dyadic step function (Walnut,
 529 2013), Scale 0 can be looked at as the mean of a signal. Since the algorithm starts with
 530 the original time series, the first approximation is the data itself:

$$\tilde{a}_{m+1} = \underline{\underline{d}} \quad (\text{A5})$$

531 As a consequence, the transformation T of a time series $\underline{\underline{d}}$ for getting the scale j
 532 coefficients \tilde{d}_{ji} at scale interval i can be written as a nested linear transform

$$\tilde{d}_{ji} = G(j)_{i\alpha} \left(\prod_{l=0}^{m-j-1} \underline{\underline{H}}(m-l) \right)_{\alpha\beta} d_{\beta}, \quad (\text{A6})$$

533 where greek letters subscript the dimensions which are affected by the sum-convention.
 534 Thus, the resulting scale process is a discrete Gaussian process as well. This allows the
 535 use of the same type of DMF as in Teixeira Parente et al. (2019) for all wavelet scales.
 536 Accordingly, $\widetilde{GP}(\underline{d})$ is completely defined by the transformed data $\tilde{\underline{d}}$ and the covariance
 537 matrix $\tilde{\underline{\Gamma}}$. The relations for these quantities can be obtained by inserting the decompo-
 538 sition as in Eq. A6 into the common definitions of mean and covariance, respectively:

$$\tilde{\mu}_{ji} = \tilde{d}_{ji} = G(j)_{i\alpha} \left(\prod_{l=0}^{m-j-1} \underline{H}(m-l) \right)_{\alpha\beta} \mu_{\beta}, \quad (\text{A7})$$

$$\tilde{\Gamma}_{jiuw} = G(j)_{i\alpha} \left(\prod_{l=0}^{m-j-1} \underline{H}(m-l) \right)_{\alpha\beta} \Gamma_{\beta\gamma} G(u)_{w\delta} \left(\prod_{l=0}^{m-u-1} \underline{H}(m-l) \right)_{\delta\gamma}. \quad (\text{A8})$$

539 Here j and u are subscripts for the scale. The indices i and w indicate the num-
 540 ber of the coefficient within a scale. Hence, the covariance matrix $\tilde{\underline{\Gamma}}$ can be looked at as
 541 a four dimensional matrix describing the m scale-covariance matrices and the covariance
 542 between them for $j \neq u$. For the Haar-Wavelet the matrix is sparse with some special
 543 properties for diagonal matrices $\underline{\Gamma}$ which arise from \underline{H} and \underline{G} . For further information
 544 about this, we refer to studies of such covariance matrices as in Vannucci and Corradi
 545 (1999). It can be shown that for a decomposition as in Eq. A8, $\tilde{\underline{\Gamma}}$ is a constant diago-
 546 nal matrix if $\underline{\Gamma}$ is. Hence, $\tilde{\underline{\Gamma}}$ is equal to the lumped matrix $\hat{\underline{\Gamma}}$. Since the Haar system pro-
 547 vides orthogonal basis functions and, hence, the decomposition in Eq. A8 is a nested or-
 548 thogonal change of basis, our constant diagonal covariance matrix even remains unchanged.
 549 This obviates the need for decomposing the covariance matrix for independent homoscedas-
 550 tic errors:

$$\hat{\underline{\Gamma}} = \tilde{\underline{\Gamma}} = \underline{\Gamma}. \quad (\text{A9})$$

551 Inserting Eq. A9 in Eq. 6 the WMI of the homoscedastic Gaussian measurement
 552 error computes to zero. The scales can be assumed to be independent from each other.
 553 Recall the assumption of an homoscedastic measurement error within 2.1.2. For heteroscedas-
 554 tic errors $\tilde{\underline{\Gamma}}$ might be sparse but not diagonal and consequently not equal to $\hat{\underline{\Gamma}}$ anymore
 555 - even for the Haar-Wavelet. There would be m off-diagonal diagonals. As a consequence
 556 the DMFs could only be defined approximately.

557 Appendix B Model equations

558 LuKARS is based on the implementation of hydrotopes. Each hydrotope i repre-
 559 sents a distinct bucket that is balanced for each time step n using the following equa-
 560 tion:

$$E_{i,n+1} = \max[0, E_{i,n} + (S_{i,n} - \frac{Q_{\text{hyd},i,n} + Q_{\text{sec},i,n} + Q_{\text{is},i,n}}{a_i}) \Delta t] \quad (\text{B1})$$

561 Here, E_i represents the water level [L] in hydrotope i . S_i is the mass balance of all
 562 possible sinks and sources in a recharge area, in our case the mass balance of precipi-
 563 tation, snow melt, evapotranspiration and interception. For our case study, we use in-
 564 terception estimates provided in DVWK (1996). Further, snow melt and retention are
 565 considered using a temperature index model proposed by Martinec (1960). Finally, evap-
 566 otranspiration is computed using the method of Thornthwaite (1948). Each hydrotope
 567 i has three flow components, i.e. the quickflow ($Q_{\text{hyd},i}$ [L^3T^{-1}]), secondary spring dis-
 568 charge ($Q_{\text{sec},i}$ [L^3T^{-1}]) and groundwater recharge ($Q_{\text{is},i}$ [L^3T^{-1}]). The absolute area cov-
 569 ered by a hydrotope is given by a_i [L^2].

570 The groundwater recharge is transferred to the baseflow storage B , for which the
 571 following balance equation is solved for each time step n :

$$E_{b,n+1} = \max[0, E_{b,n} + (\frac{\Sigma(Q_{is,i,n}) - Q_{b,n}}{A}) \Delta t] \quad (\text{B2})$$

572 The water level [L] in the baseflow storage is defined as E_b . The sum of the ground-
 573 water recharge coming from each hydrotope is indicated by $\Sigma(Q_{is,i})$ [L^3T^{-1}]. Then, the
 574 Q_b [L^3T^{-1}] represents the flow from storage B to the spring, representing the baseflow
 575 from the phreatic aquifer. The absolute area of the recharge area is given by A [L^2].

576 In LuKARS, the quickflow $Q_{\text{hyd},i}$ is computed based on a non-linear transfer func-
 577 tion, which we define as follows:

$$Q_{\text{hyd},i,n} = a_i \frac{k_{\text{hyd},i}}{l_{\text{hyd},i}} \varepsilon_n \left[\frac{\max(0, E_{i,n} - E_{\min,i})}{E_{\max,i} - E_{\min,i}} \right]^{\alpha_i} \quad (\text{B3})$$

578 Here, $E_{\max,i}$ [L] and $E_{\min,i}$ [L] are the upper and lower storage thresholds of hy-
 579 drotope i . The specific discharge parameter for the quickflow is given by $k_{\text{hyd},i}$ [L^2T^{-1}].
 580 $l_{\text{hyd},i}$ [L] represents the mean distance of hydrotope i to the spring, thus, accounting for
 581 the relative location of a specific hydrotope in a recharge area. The ratio between $k_{\text{hyd},i}$
 582 and $l_{\text{hyd},i}$ indicates the hydrotope discharge coefficient. A hydrotope-specific exponent
 583 of the quickflow is given by α_i . Finally, the dimensionless connectivity/activation indi-
 584 cator ε defines whether $Q_{\text{hyd},i}$ is active or not. It is defined as

$$\varepsilon_{n+1} = 0 \text{ if } \begin{cases} \varepsilon_n = 0 \ \& \ E_{i,n+1} < E_{\max,i} \ \text{or} \\ \varepsilon_n = 1 \ \& \ E_{i,n+1} \leq E_{\min,i} \end{cases} \quad (\text{B4})$$

$$\varepsilon_{n+1} = 1 \text{ if } \begin{cases} \varepsilon_n = 0 \ \& \ E_{i,n+1} \geq E_{\max,i} \text{ or} \\ \varepsilon_n = 1 \ \& \ E_{i,n+1} > E_{\min,i} \end{cases} \quad (\text{B5})$$

585 All other flow components are calculated using linear transfer laws, i.e.

$$Q_{\text{sec},i,n} = a_i k_{\text{sec},i} \max(0, E_{i,n} - E_{\text{sec},i}) \quad (\text{B6})$$

$$Q_{\text{is},i,n} = a_i k_{\text{is},i} E_{i,n} \quad (\text{B7})$$

586 and

$$Q_{\text{b},n} = A k_{\text{b}} E_{\text{b},n} \quad (\text{B8})$$

587 where $E_{\text{sec},i}$ [L] represents the activation level for a secondary spring discharge. $k_{\text{sec},i}$
 588 [LT^{-1}], $k_{\text{is},i}$ [LT^{-1}] and k_{b} [LT^{-1}] indicate the discharge parameters of $Q_{\text{sec},i}$ [L^3T^{-1}],
 589 $Q_{\text{is},i}$ [L^3T^{-1}] and Q_{b} [L^3T^{-1}], respectively.

590 Appendix C Statistical independence of LuKARS model parameters

591 Depending on the specific physical characteristics of each LuKARS hydrotope, their
 592 respective parameters need to be considered dependently. This means, e.g., if a hydro-
 593 tope has shallow soils with coarse grained soil texture, it should have lower values for
 594 storage parameters as compared to deep and fine-textured soils. For that reason, we need
 595 to introduce the following parameter constraints, i.e. the dependencies between each hy-
 596 drotope:

$$\begin{aligned}
k_{\text{hyd},1} &\geq k_{\text{hyd},2} \geq k_{\text{hyd},3}, \\
E_{\text{min},1} &\leq E_{\text{min},2} \leq E_{\text{min},3}, \\
E_{\text{max},1} &\leq E_{\text{max},2} \leq E_{\text{max},3}, \\
\alpha_1 &\geq \alpha_2 \geq \alpha_3, \\
k_{\text{is},1} &\geq k_{\text{is},2} \geq k_{\text{is},3}, \\
k_{\text{sec},1} &\geq k_{\text{sec},2} \geq k_{\text{sec},3}, \\
E_{\text{sec},1} &\leq E_{\text{sec},2} \leq E_{\text{sec},3}.
\end{aligned} \tag{C1}$$

597 These constraints lead to a statistical dependence between the hydrotope model
598 parameters. However, to use the active subspace method, statistically independent pa-
599 rameters are required. Hence, we need to introduce a set of calibration parameters to
600 overcome this limitation. Here, we define three types of non-normalized calibration pa-
601 rameters with parameter density ρ , which can be chosen based on prior knowledge about
602 the respective parameters. For the ranges of all discharge parameters, i.e. k_{hyd} , k_{is} and
603 k_{sec} (in the following referred to as k_* parameters), we assumed a logarithmic distribu-
604 tion ρ . In contrast, a uniform prior distribution was assumed for all other calibration
605 parameters.

606 To take into account the log distribution of the k_* parameters, we define

$$k_*^{\text{log}} = \log(k_*) \tag{C2}$$

607 for each $k_* \in \{k_{\text{hyd},i}, k_{\text{is},i}, k_{\text{sec},i}\}$, $i = 1, 2, 3$.

608 Since $E_{\text{min},i} \leq E_{\text{max},i}$ for in all hydrotopes, $E_{\text{max},i}$ is always dependent on sam-
609 ples taken for $E_{\text{min},i}$. Hence, we define $E_{\text{max},i} = E_{\text{min},i} + \Delta E_i$ and replace $E_{\text{max},i}$ by
610 ΔE_i . Then, ΔE_i is independent of $E_{\text{min},i}$.

611 To further consider the differences between two successive hydrotopes, we define
 612 new (non-normalized) calibration parameters. In the following, parameters indicated with
 613 a Δ represent new normalized calibration parameters. They take values in $[0,1]$ and re-
 614 place their corresponding model parameters. It has to be ensured that the calibration
 615 parameters are selected such that their corresponding model parameters are within their
 616 predefined ranges.

$$\begin{aligned}
 k_{\text{hyd},i}^{\log} &= k_{\text{hyd},i,\text{lb}}^{\log} + \Delta k_{\text{hyd},(i-1),i}^{\log} (\min\{k_{\text{hyd},i,\text{ub}}^{\log}, k_{\text{hyd},i-1}^{\log}\} - k_{\text{hyd},i,\text{lb}}^{\log}), \\
 E_{\text{min},i} &= \max\{E_{\text{min},i-1}, E_{\text{min},i,\text{lb}}\} \\
 &\quad + \Delta E_{\text{min},(i-1),i} (E_{\text{min},i,\text{ub}} - \max\{E_{\text{min},i-1}, E_{\text{min},i,\text{lb}}\}), \\
 \alpha_i &= \alpha_{i,\text{lb}} + \Delta \alpha_{(i-1),i} (\min\{\alpha_{i,\text{ub}}, \alpha_{i-1}\} - \alpha_{i,\text{lb}}), \\
 k_{\text{is},i}^{\log} &= k_{\text{is},i,\text{lb}}^{\log} + \Delta k_{\text{is},(i-1),i}^{\log} (\min\{k_{\text{is},i,\text{ub}}^{\log}, k_{\text{is},i-1}^{\log}\} - k_{\text{is},i,\text{lb}}^{\log}), \\
 k_{\text{sec},i}^{\log} &= k_{\text{sec},i,\text{lb}}^{\log} + \Delta k_{\text{sec},(i-1),i}^{\log} (\min\{k_{\text{sec},i,\text{ub}}^{\log}, k_{\text{sec},i-1}^{\log}\} - k_{\text{sec},i,\text{lb}}^{\log}), \\
 E_{\text{sec},i} &= \max\{E_{\text{sec},i-1}, E_{\text{sec},i,\text{lb}}\} \\
 &\quad + \Delta E_{\text{sec},(i-1),i} (E_{\text{sec},i,\text{ub}} - \max\{E_{\text{sec},i-1}, E_{\text{sec},i,\text{lb}}\}),
 \end{aligned} \tag{C3}$$

617 The lower bounds (_{lb}) and upper bounds (_{ub}) of each model parameter interval are
 618 defined in Table 1. In our case, Hyd 1 acts as the reference hydrotope. Thus, we need
 619 to introduce new synthetic parameters only for the other hydrotopes, i.e. Hyd 2 and 3.
 620 Moreover, all non-normalized calibration parameters are normalized. This means that
 621 they are mapped to the interval $[-1,1]$. Given the described normalization methodology,
 622 we define the final 21-dimensional vector \mathbf{x} of calibration parameters as follows:

$$\begin{aligned}
\mathbf{x} = & (\bar{k}_{\text{hyd},1}^{\text{log}}, \bar{E}_{\text{min},1}, \Delta \bar{E}_1, \alpha_1, \bar{k}_{\text{is},1}, \bar{k}_{\text{sec},1}, \bar{E}_{\text{sec},1}, \\
& \Delta \bar{k}_{\text{hyd},(1,2)}^{\text{log}}, \Delta \bar{E}_{\text{min},(1,2)}, \Delta \bar{E}_2, \Delta \bar{\alpha}_{(1,2)}, \\
& \Delta \bar{k}_{\text{is},(1,2)}, \Delta \bar{k}_{\text{sec},(1,2)}, \Delta \bar{E}_{\text{sec},(1,2)}, \\
& \Delta \bar{k}_{\text{hyd},(2,3)}^{\text{log}}, \Delta \bar{E}_{\text{min},(2,3)}, \Delta \bar{E}_3, \Delta \bar{\alpha}_{(2,3)}, \\
& \Delta \bar{k}_{\text{is},(2,3)}, \Delta \bar{k}_{\text{sec},(2,3)}, \Delta \bar{E}_{\text{sec},(2,3)})^\top \in \mathbf{R}^{21}.
\end{aligned} \tag{C4}$$

623 Acknowledgments

624 This collaborative research is a result of the UNMIX project (UNcertainties due to bound-
625 ary conditions in predicting MIXing in groundwater), which is supported by the Deutsche
626 Forschungsgemeinschaft (DFG) through the TUM International Graduate School for Sci-
627 ence and Engineering (IGSSE), GSC 81. Daniel Bittner and Gabriele Chiogna refer to
628 the Interreg Central Europe project boDEREC-CE funded by ERDF. Daniel Bittner and
629 David Labat acknowledge financial support in form of the Procope scholarship by the
630 French Ministry of Europe and Foreign Affairs. Gabriele Chiogna further acknowledges
631 the support of the Stiftungsfonds für Umweltökonomie und Nachhaltigkeit GmbH (SUN).
632 Additional financial support for Gabriele Chiogna and Barbara Wohlmuth was provided
633 by the German Research Foundation (DFG) in the Project Hydromix (WO671/11-1).
634 The authors further thank the water works Waidhofen a.d. Ybbs for providing the rel-
635 evant spatial and time series data. Datasets and source codes for this research are avail-
636 able in this in-text data citation reference: Bittner, Engel, et al. (2020) (shared under
637 the Creative Commons Attribution CC BY).

638 References

639 Adamowski, J., & Prokoph, A. (2014). Determining the amplitude and timing of
640 streamflow discontinuities: A cross wavelet analysis approach. *Hydrological*
641 *processes*, 28(5), 2782–2793.

- 642 Agarwal, A., Maheswaran, R., Sehgal, V., Khosa, R., Sivakumar, B., & Bernhofer,
643 C. (2016). Hydrologic regionalization using wavelet-based multiscale entropy
644 method. *Journal of Hydrology*, *538*, 22–32.
- 645 Arnold, J. G., Srinivasan, R., Muttiah, R. S., & Williams, J. R. (1998). Large area
646 hydrologic modeling and assessment part i: model development 1. *JAWRA*
647 *Journal of the American Water Resources Association*, *34*(1), 73–89.
- 648 Beven, K. (1995). Linking parameters across scales: subgrid parameterizations and
649 scale dependent hydrological models. *Hydrological processes*, *9*(5-6), 507–525.
- 650 Bittner, D., Engel, M., Wohlmuth, B., Labat, D., & Chiogna, G. (2020). Discrete
651 wavelet transform coupled with the active subspace method. *HydroShare*. doi:
652 <https://doi.org/10.4211/hs.4901a0d654334c259f4ff9b49dc0a74e>
- 653 Bittner, D., Narany, T. S., Kohl, B., Disse, M., & Chiogna, G. (2018). Modeling the
654 hydrological impact of land use change in a dolomite-dominated karst system.
655 *Journal of Hydrology*, *567*, 267–279.
- 656 Bittner, D., Rychlik, A., Klöffel, T., Leuteritz, A., Disse, M., & Chiogna, G. (2020).
657 A gis-based model for simulating the hydrological effects of land use changes
658 on karst systems—the integration of the lukars model into freewat. *Environmental*
659 *Modelling & Software*, 104682.
- 660 Bittner, D., Teixeira Parente, M., Mattis, S., Wohlmuth, B., & Chiogna, G. (2020).
661 Identifying relevant hydrological and catchment properties in active subspaces:
662 An inference study of a lumped karst aquifer model. *Advances in Water Re-*
663 *sources*, *135*, 103472.
- 664 Borgonovo, E., Lu, X., Plischke, E., Rakovec, O., & Hill, M. C. (2017). Making the
665 most out of a hydrological model data set: Sensitivity analyses to open the
666 model black-box. *Water Resources Research*, *53*(9), 7933–7950.
- 667 Carey, S. K., Tetzlaff, D., Buttle, J., Laudon, H., McDonnell, J., McGuire, K., . . .
668 Shanley, J. (2013). Use of color maps and wavelet coherence to discern sea-
669 sonal and interannual climate influences on streamflow variability in northern

- 670 catchments. *Water Resources Research*, *49*(10), 6194–6207.
- 671 Charlier, J.-B., Ladouche, B., & Maréchal, J.-C. (2015). Identifying the impact of
672 climate and anthropic pressures on karst aquifers using wavelet analysis. *Journal of Hydrology*, *523*, 610–623.
- 673
- 674 Chiogna, G., Marcolini, G., Liu, W., Pérez Ciria, T., & Tuo, Y. (2018). Coupling
675 hydrological modeling and support vector regression to model hydropeaking in
676 alpine catchments. *Science of The Total Environment*, *633*, 220–229.
- 677 Cloke, H., Pappenberger, F., & Renaud, J.-P. (2008). Multi-method global sensitiv-
678 ity analysis (mmgsa) for modelling floodplain hydrological processes. *Hydrolog-
679 ical Processes: An International Journal*, *22*(11), 1660–1674.
- 680 Constantine, P. G., & Diaz, P. (2017). Global sensitivity metrics from active sub-
681 spaces. *Reliability Engineering & System Safety*, *162*, 1–13.
- 682 Constantine, P. G., Dow, E., & Wang, Q. (2014). Active subspace methods in
683 theory and practice: applications to kriging surfaces. *SIAM J. Sci. Comput.*,
684 *36*(4), A1500–A1524. doi: 10.1137/130916138
- 685 Coulibaly, P., & Burn, D. H. (2004). Wavelet analysis of variability in annual cana-
686 dian streamflows. *Water Resources Research*, *40*(3).
- 687 Cover, T. M., & Thomas, J. A. (2012). *Elements of information theory*. John Wiley
688 & Sons.
- 689 Daubechies, I. (1990). The wavelet transform, time-frequency localization and signal
690 analysis. *IEEE transactions on information theory*, *36*(5), 961–1005.
- 691 Duran, L., Massei, N., Lecoq, N., Fournier, M., & Labat, D. (2020). Analyzing
692 multi-scale hydrodynamic processes in karst with a coupled conceptual model-
693 ing and signal decomposition approach. *Journal of Hydrology*, *583*, 124625.
- 694 DVWK. (1996). Ermittlung der Verdunstung von Land- und Wasserflächen.
695 *DVWK-Merkblatt*, *238/1996*.
- 696 Erdal, D., & Cirpka, O. A. (2019). Global sensitivity analysis and adaptive stochas-
697 tic sampling of a subsurface-flow model using active subspaces. *Hydrology and*

- 698 *Earth System Sciences*, 23(9), 3787–3805.
- 699 Erdal, D., & Cirpka, O. A. (2020). Improved sampling of behavioral subsurface
700 flow model parameters using active subspaces. *Hydrology and Earth System
701 Sciences Discussions*, 1–12.
- 702 Gilbert, J. M., Jefferson, J. L., Constantine, P. G., & Maxwell, R. M. (2016). Global
703 spatial sensitivity of runoff to subsurface permeability using the active sub-
704 space method. *Advances in water resources*, 92, 30–42.
- 705 Grinsted, A., Moore, J. C., & Jevrejeva, S. (2004). Application of the cross wavelet
706 transform and wavelet coherence to geophysical time series. *Nonlinear Pro-
707 cesses in Geophysics*, 11(5/6), 561–566.
- 708 Hartmann, A., Barberá, J. A., & Andreo, B. (2017). On the value of water qual-
709 ity observations for karst model parameterization. *Hydrol. Earth Syst. Sci.*, 21,
710 5971–5985.
- 711 Jefferson, J. L., Gilbert, J. M., Constantine, P. G., & Maxwell, R. M. (2015). Active
712 subspaces for sensitivity analysis and dimension reduction of an integrated
713 hydrologic model. *Computers & Geosciences*, 83, 127–138.
- 714 Jennings, K., & Jones, J. A. (2015). Precipitation-snowmelt timing and snowmelt
715 augmentation of large peak flow events, western c ascades, oregon. *Water Re-
716 sources Research*, 51(9), 7649–7661.
- 717 Labat, D. (2005). Recent advances in wavelet analyses: Part 1. a review of concepts.
718 *Journal of Hydrology*, 314(1-4), 275–288.
- 719 Labat, D., Ababou, R., & Mangin, A. (2000a). Rainfall–runoff relations for karstic
720 springs. part i: convolution and spectral analyses. *Journal of hydrology*, 238(3-
721 4), 123–148.
- 722 Labat, D., Ababou, R., & Mangin, A. (2000b). Rainfall–runoff relations for karstic
723 springs. part ii: continuous wavelet and discrete orthogonal multiresolution
724 analyses. *Journal of hydrology*, 238(3-4), 149–178.
- 725 Larocque, M., Mangin, A., Razack, M., & Banton, O. (1998). Contribution of cor-

- 726 relation and spectral analyses to the regional study of a large karst aquifer
727 (charente, france). *Journal of hydrology*, 205(3-4), 217–231.
- 728 Mallat, S. G. (1989). A theory for multiresolution signal decomposition: the wavelet
729 representation. *IEEE transactions on pattern analysis and machine intelli-*
730 *gence*, 11(7), 674–693.
- 731 Mangin, A. (1984). Pour une meilleure connaissance des systèmes hydrologiques à
732 partir des analyses corrélatoire et spectrale. *Journal of hydrology*, 67(1-4), 25–
733 43.
- 734 Marcolini, G., Bellin, A., Disse, M., & Chiogna, G. (2017). Variability in snow depth
735 time series in the adige catchment. *Journal of Hydrology: Regional Studies*, 13,
736 240–254.
- 737 Martinec, J. (1960). The degree-day factor for snowmelt runoff forecasting. *IUGG*
738 *General Assembly of Helsinki, IAHS Commission of Surface Waters*, 51, 468–
739 477.
- 740 Massei, N., Laignel, B., Deloffre, J., Mesquita, J., Motelay, A., Lafite, R., & Durand,
741 A. (2010). Long-term hydrological changes of the seine river flow (france)
742 and their relation to the north atlantic oscillation over the period 1950–2008.
743 *International journal of Climatology*, 30(14), 2146–2154.
- 744 Nalley, D., Adamowski, J., & Khalil, B. (2012). Using discrete wavelet transforms
745 to analyze trends in streamflow and precipitation in quebec and ontario (1954–
746 2008). *Journal of Hydrology*, 475, 204–228.
- 747 Nalley, D., Adamowski, J., Khalil, B., & Biswas, A. (2016). Inter-annual to inter-
748 decadal streamflow variability in quebec and ontario in relation to dominant
749 large-scale climate indices. *Journal of hydrology*, 536, 426–446.
- 750 Narany, T. S., Bittner, D., Disse, M., & Chiogna, G. (2019). Spatial and temporal
751 variability in hydrochemistry of a small-scale dolomite karst environment. *En-*
752 *vironmental Earth Sciences*, 78(9), 273.
- 753 Pérez Ciria, T., & Chiogna, G. (2020). Intra-catchment comparison and classifi-

- 754 cation of long-term streamflow variability in the alps using wavelet analysis.
755 *Journal of Hydrology*, 124927.
- 756 Pérez Ciria, T., Labat, D., & Chiogna, G. (2019). Detection and interpretation
757 of recent and historical streamflow alterations caused by river damming and
758 hydropower production in the adige and inn river basins using continuous, dis-
759 crete and multiresolution wavelet analysis. *Journal of Hydrology*, 578, 124021.
- 760 Pianosi, F., Beven, K., Freer, J., Hall, J. W., Rougier, J., Stephenson, D. B., & Wa-
761 gener, T. (2016). Sensitivity analysis of environmental models: A systematic
762 review with practical workflow. *Environmental Modelling & Software*, 79,
763 214–232.
- 764 Rathinasamy, M., Khosa, R., Adamowski, J., Ch, S., Partheepan, G., Anand, J., &
765 Narsimlu, B. (2014). Wavelet-based multiscale performance analysis: An ap-
766 proach to assess and improve hydrological models. *Water Resources Research*,
767 50(12), 9721–9737.
- 768 Razavi, S., & Gupta, H. V. (2015). What do we mean by sensitivity analysis? the
769 need for comprehensive characterization of “global” sensitivity in e arth and e
770 nvironmental systems models. *Water Resources Research*, 51(5), 3070–3092.
- 771 Reinecke, R., Foglia, L., Mehl, S., Herman, J. D., Wachholz, A., Trautmann, T., &
772 Döll, P. (2019). Spatially distributed sensitivity of simulated global ground-
773 water heads and flows to hydraulic conductivity, groundwater recharge, and
774 surface water body parameterization. *Hydrology & Earth System Sciences*,
775 23(11).
- 776 Rossetto, R., De Filippis, G., Borsi, I., Foglia, L., Cannata, M., Criollo, R., &
777 Vázquez-Suñé, E. (2018). Integrating free and open source tools and dis-
778 tributed modelling codes in gis environment for data-based groundwater man-
779 agement. *Environmental Modelling & Software*, 107, 210–230.
- 780 Ryan, Ø., Ryan, & Peters. (2019). *Linear algebra, signal processing, and wavelets—a*
781 *unified approach*. Springer.

- 782 Saltelli, A., Aleksankina, K., Becker, W., Fennell, P., Ferretti, F., Holst, N., . . . Wu,
783 Q. (2019). Why so many published sensitivity analyses are false: A systematic
784 review of sensitivity analysis practices. *Environmental modelling & software*,
785 *114*, 29–39.
- 786 Saltelli, A., Ratto, M., Andres, T., Campolongo, F., Cariboni, J., Gatelli, D., . . .
787 Tarantola, S. (2008). *Global sensitivity analysis: the primer*. John Wiley &
788 Sons.
- 789 Sang, Y.-F., Wang, Z., & Liu, C. (2013). Discrete wavelet-based trend identification
790 in hydrologic time series. *Hydrological Processes*, *27*(14), 2021–2031.
- 791 Schaeffli, B., Maraun, D., & Holschneider, M. (2007). What drives high flow events
792 in the swiss alps? recent developments in wavelet spectral analysis and their
793 application to hydrology. *Advances in Water Resources*, *30*(12), 2511–2525.
- 794 Schaeffli, B., & Zehe, E. (2009). Hydrological model performance and parameter
795 estimation in the wavelet-domain. *Hydrology and Earth System Sciences*,
796 *13*(ARTICLE), 1921–1936.
- 797 Shannon, C. E. (1948). A mathematical theory of communication. *Bell system tech-*
798 *nical journal*, *27*(3), 379–423.
- 799 Song, X., Zhang, J., Zhan, C., Xuan, Y., Ye, M., & Xu, C. (2015). Global sensitivity
800 analysis in hydrological modeling: Review of concepts, methods, theoretical
801 framework, and applications. *Journal of hydrology*, *523*, 739–757.
- 802 Tang, Y., Reed, P., Wagener, T., & van Werkhoven, K. (2007). Comparing sensi-
803 tivity analysis methods to advance lumped watershed model identification and
804 evaluation. *Hydrology and Earth System Sciences*, *11*(2), 793–817.
- 805 Teixeira Parente, M., Bittner, D., Mattis, S. A., Chiogna, G., & Wohlmuth, B.
806 (2019). Bayesian calibration and sensitivity analysis for a karst aquifer model
807 using active subspaces. *Water Resources Research*, *55*(8), 7086–7107.
- 808 Thornthwaite, C. W. (1948). *An approach toward a rational classification of climate*
809 (Vol. 66) (No. 1). LWV.

- 810 Torrence, C., & Compo, G. P. (1998). A practical guide to wavelet analysis. *Bulletin*
811 *of the American Meteorological society*, 79(1), 61–78.
- 812 Vannucci, M., & Corradi, F. (1999). Covariance structure of wavelet coefficients:
813 theory and models in a bayesian perspective. *Journal of the Royal Statistical*
814 *Society: Series B (Statistical Methodology)*, 61(4), 971–986.
- 815 van Werkhoven, K., Wagener, T., Reed, P., & Tang, Y. (2008). Characterization
816 of watershed model behavior across a hydroclimatic gradient. *Water Resources*
817 *Research*, 44(1).
- 818 Vrugt, J. A., Bouten, W., Gupta, H. V., & Sorooshian, S. (2002). Toward improved
819 identifiability of hydrologic model parameters: The information content of
820 experimental data. *Water Resources Research*, 38(12), 48–1.
- 821 Wagener, T., & Montanari, A. (2011). Convergence of approaches toward reduc-
822 ing uncertainty in predictions in ungauged basins. *Water Resources Research*,
823 47(6).
- 824 Wagener, T., & Pianosi, F. (2019). What has global sensitivity analysis ever done
825 for us? a systematic review to support scientific advancement and to inform
826 policy-making in earth system modelling. *Earth-science reviews*.
- 827 Walnut, D. F. (2013). *An introduction to wavelet analysis*. Springer Science & Busi-
828 ness Media.
- 829 Yang, C., Yu, Z., Hao, Z., Zhang, J., & Zhu, J. (2012). Impact of climate change
830 on flood and drought events in huaihe river basin, china. *Hydrology Research*,
831 43(1-2), 14–22.
- 832 Zolezzi, G., Bellin, A., Bruno, M., Maiolini, B., & Siviglia, A. (2009). Assessing hy-
833 drological alterations at multiple temporal scales: Adige river, italy. *Water Re-*
834 *sources Research*, 45(12).